Enhancing Biocompatibility and Antibacterial Activity of Ti6Al4V by entrapping Ag and Hydroxyapatite inside alginate filled pores of TiO_2 layer grown by spark anodizing

Davide Pupillo[a], *Andrea Zaffora*[b,*], *Francesco Di Franco*[b], *Pasquale Picone*[c,d], *Domenico Nuzzo*[c,d], *Monica Santamaria*[b,*]

[a]Politecnico di Torino, Dipartimento di Scienza Applicata e Tecnologia, Corso Duca degli Abruzzi 24, 10129 Torino, Italy

[b]Università degli Studi di Palermo, Dipartimento di Ingegneria, Viale delle Scienze, Ed. 6, 90128 Palermo, Italy

[c]Istituto per la Ricerca e l'Innovazione Biomedica, Consiglio Nazionale delle Ricerche, 90146 Palermo, Italy

[d]Università degli Studi di Palermo, Dipartimento di Scienze e Tecnologie Biologiche Chimiche e Farmaceutiche, Viale delle Scienze, Ed. 16, 90128, Palermo, Italy

*corresponding authors: monica.santamaria@unipa.it, andrea.zaffora@unipa.it

Co-authors e-mail address: davide.pupillo@polito.it; francesco.difranco@unipa.it; pasquale.picone@irib.cnr.it; domenico.nuzzo@irib.cnr.it

Abstract

A three-step electrochemical process was developed to grow a coating on Ti6Al4V alloy for biomedical applications aimed to enhance its bioactivity. The coating was composed by a porous titanium oxide filled with Ag, alginic acid and hydroxyapatite to provide antibacterial properties and, at the same time, osteointegration capability. Anodized and treated with the electrochemical process samples were characterized by Scanning Electron Microscopy (SEM), Energy-Dispersive X-ray Spectroscopy (EDX), X-Ray Diffraction and Raman Spectroscopy to have information about morphology and composition soon after the fabrication and after immersion in Hanks' solution. Bioactivity of the samples was also proved by electrochemical tests through Electrochemical Impedance Spectroscopy (EIS) measurements. Antibacterial properties, cytocompatibility and hemocompatibility of the samples were successfully demonstrated by *in vitro* tests.

Keywords: Ti alloys; bioactivity; hydroxyapatite; antibacterial activity; Ag; alginate

Introduction

Biomedical materials are widely studied to be used as structures or implants in human body to replace damaged hard and soft tissues. Those materials used as implants for load-bearing applications must comply several features to be durable and reliable, such as high corrosion resistance and mechanical strength, biocompatibility and good osteointegration to avoid revision surgery [1].

Based on these characteristics, metals and metallic alloys are used as implants for load-bearing applications. Among many others, Co-Cr alloys, stainless steels, Ti and Ti alloys are widely used for several biomedical applications. In particular, Ti and its alloys have elastic moduli close to those of bones and lower density with respect to that of Co-Cr alloys and stainless steels [2,3]. Furthermore, compared to pure Ti, Ti alloys have higher mechanical properties which make them particularly suitable for orthopaedic and traumatology implants. However, Ti and Ti alloys are considered bioinert materials, i.e. they do not react (chemically or biologically) with surrounding tissues in the human body [4]. Moreover, corrosion phenomena involving Ti alloy, namely Ti6Al4V alloy, can lead to the release of Al and V alloys that are considered hazardous elements for human body.

In order to promote osteointegration of implants with existing human bone tissue, thus to optimize the integration of the device, coatings growth on implant surface can be a suitable way. In particular, for Ti and Ti Alloys, spark anodizing can represent a suitable technique to grow strongly adherent porous ceramic coatings to the substrate, minimizing possible spalling phenomena that can be the cause of osteolysis.

In this context, several strategies have been investigated to enhance the bioactivity of Ti alloys and thus their osteointegration [5–7]. It is well documented in literature that the presence of hydroxyapatite (HA, $Ca_{10}(PO_4)_6(OH)_2$) can enhance the osteointegration of foreign biomaterials due to its high biocompatibility with hard and soft tissues [8]. Therefore, inducing the incorporation or the growth of HA has been revealed as a good strategy to improve the materials bioactivity. This

can be reached, for instance, by an electrochemical conversion coating process as spark anodizing by precisely tailoring the operating conditions (formation voltage, electrolyte bath composition, etc.) [3,9,10]. Moreover, the growth of a thick anodic layer on the surface of Ti6Al4V alloy can enhance its corrosion resistance in body fluids and reduce the release of Al and V during the service life of the implant.

Another crucial characteristic of biomaterials to be used as implants is the presence of antibacterial agents. This is a key point to avoid the proliferation of bacteria and other microorganisms into the implant leading to possible infection during the healing period. Ag is one of the most studied metals as antibacterial agent due to its antibacterial capacity, relative cheapness and availability and its high activity against a wide range of microorganisms as microbes and parasites [11].

In this work we want to design a multi-step process aimed to simultaneously enhance biocompatibility and antibacterial activity of Ti6Al4V alloys for biomedical applications. This multilayer coating and the three-step electrochemical process can be advantageous from many points of view. Every single step is important to give to the final coating the desired properties, i.e. antibacterial and biocompatibility properties. The anodizing process allows to cover the alloy surface with a thick porous and well adherent TiO_2 layer to hinder Al and V release, to improve surface wettability and to provide a high specific surface for accelerating HA growth rate. Such porous film provides a good pattern for hosting Ag to provide antibacterial properties, whose release rate in turn is slowed down due to the sealing of pores with a HA-containing alginic acid gel deposited during the electrophoresis deposition (EPD). This step is very important because the gel can uptake electrolyte during immersion, thus Ag can still fulfill its antibacterial action but, at the same time, its release is slowed down so that cannot be cytotoxic (as Ag could be if the release rate is particularly high). And, finally, the presence of HA provide the seed for further HA growth and, thus, can lead to a better osteointegration.

Therefore, the three-step electrochemical process provides a route for a smart functionalization of Ti6Al4V alloys. Moreover, this process can be fully scaled at the industrial level and can help in decarbonizing the fabrication industrial processes.

The success of this multifunctional coating is studied by evaluating the morphological/compositional changes after the surface treatment by using Scanning Electron Microscopy (SEM), Energy-Dispersive X-ray Spectroscopy (EDX), and Raman spectroscopy. Electrochemical tests (Electrochemical Impedance Spectroscopy measurements and polarization curves) are carried out in Hanks' solution at 37°C to evaluate coating corrosion resistance. Finally, *in vitro* tests are necessary to study cytocompatibility, antibacterial activity and hemocompatibility of the surface-modified Ti6Al4V alloy.

Experimental

Materials

Ti6Al4V titanium alloy with a dimension of 45 × 20 mm and a thickness of 2 mm was used. The samples were mechanically polished using SiC abrasive papers with P800, P1200 and P2400 grit. Subsequently, the samples were degreased using acetone by using an ultrasonic bath and then were rinsed with deionized water.

Anodic treatment

Ti6Al4V alloys were anodized in 0.2 M calcium acetate (CA, $(CH_3COO)_2Ca \cdot H_2O$) and 0.04 M β-glycerol phosphate disodium pentahydrate (β-GPDS, $C_3H_7Na_2O_6P \cdot 5H_2O$) aqueous solution. A two-electrode configuration was used where the alloy was the anode (working electrode) and a Pt net having a very high specific area the cathode (counter electrode). Anodic oxide growth was carried out galvanostatically at 20 mA cm^{-2} and the voltage compliance was set to 200 V.

Electrodeposition

Electrodeposition process was carried out with a three-electrode configuration, where Ti alloy was the working electrode, a Pt net having a very high specific area was the counter electrode and a silver/silver chloride/KCl (U_0 = 0.197 V vs SHE) was the reference electrode. The electrolyte was a 0.1 M $AgNO_3$ (pH = 4.5) aqueous solution. The electrodeposition was carried out galvanostatically at 1 mA cm^{-2} for 2 s.

Electrophoretic deposition

The bath for the EPD process was prepared by dissolving the sodium alginate, with a concentration of 4 g l^{-1}, in deionized water for 10 min. Then the solution was additionally treated in an ultrasonic bath for 10 min and was also stirred at 600 rpm for 5 min [4] . Ethanol was added to the solution in a ratio of 4/6 with respect to deionized water. Afterwards, HA (1 g l^{-1}) particles were slowly added to the solution and the pH was adjusted to 7.9 by the addition of NaOH. The EPD process was carried out in a two-electrode configuration with continuous stirring at 100 rpm. A stainless steel sheet (AISI 316L) was used as counter electrode. EPD process was carried out potentiostatically at 7 V for 7 minutes.

SEM, EDX, XRD and Raman Spectroscopy analysis

Samples morphology was investigated with a FEI Quanta 200 FEG SEM microscope coupled with Energy-Dispersive X-ray Spectrum (EDX) facility. Each sample was covered with a thin Au film deposited by sputtering before any investigation. X-ray diffraction (XRD) measurements were performed using a Pan Analytical Empyrean diffractometer with a Cu anode (Cu Kα radiation, λ =

0.15405 nm) equipped with PIXCel1D detector (voltage: 40 kV, current: 40 mA). The XRD patterns were collected over the 2θ angle range: 10° - 90°.

Micro Raman analysis was performed through a Renishaw inVia Raman Microscope spectrometer equipped with a microprobe (50x) and a CCD detector with a Nd:YAG laser with a wavelength of 532 nm.

Electrochemical characterization

Electrochemical Impedance Spectroscopy (EIS) data were recorded using a Parstat 2263 (PAR), connected to a computer for the data acquisition. The amplitude of the applied sinusoidal signal was 10 mV with a frequency ranging from 100 mHz to 100 kHz. The resultant spectra were fitted via ZSimpWin software.

The three-electrode configuration was the same used for the electrodeposition process. The samples were characterized in Hanks' solution, whose composition is reported in Table 1, at 37°C.

Component	**Concentration [g l^{-1}]**
NaCl	8
KCl	0.4
$NaHCO_3$	0.35
$NaH_2PO_4 \cdot H_2O$	0.25
$Na_2HPO_4 \cdot H_2O$	0.06
$CaCl_2 \cdot 2H_2O$	0.19
$MgCl_2$	0.19
$MgSO_4 \cdot 7H_2O$	0.06
Glucose	1

Table 1. Composition of Hanks' solution (pH = 7.3).

Polarization curves were recorded with a scan rate of 2 $mV \cdot s^{-1}$, with the same three-electrode configuration, using a Parstat 2263 (Princeton Applied Research, AMETEK). OCP (Open Circuit Potential) was recorded for at least 1 h and then the polarization curve was recorded starting from −150 mV vs OCP and sweeping the electrode potential toward anodic direction up to 0.5 V vs Ag/AgCl.

Contact angle measurement

Contact angle was measured using FTA 1000 instrument, with droplets of deionized water of 5 μL. Measurements were repeated at least three times in several positions of the samples. Reported contact angle value is the mean value.

Cell culture

3T3 fibroblast cells were cultured with RPMI 1640 medium (Celbio srl, Milan, Italy) supplemented with 10% Fetal Bovine Serum (FBS) (Gibco-Invitrogen, Milan, Italy), 2 mM glutamine, 1% penicillin and 1% streptomycin (50 mg/mL). Cells were maintained in a humidified 5% CO_2 atmosphere at 37 ± 0.1 °C. For cytocompatibility assays, 3T3 cells were seeded on 96-well flat-bottom (density $4x10^3$ per well). For the release test, the samples were incubated with medium cell cultures at different times (1, 4, 7, 12 days) at 37 °C. After this incubation, the medium was collected and administered (200 μl) to 3T3 cells monolayer at 37 °C for 48 h.

Determination of cell viability

Cell viability was measured by MTS assay (Promega Italia, S.r.l., Milan, Italy). MTS [3-(4,5-dimethylthiazol-2-yl)-5-(3-carboxymethoxyphenyl)-2-(4-sulphophenyl)-2H-tetrazolium] was utilized according to the manufacturer's instructions. After treatment, 20 µL of the MTS solution were added to each well and the incubation was continued for 2 h at 37 °C in humidified incubator with 5% CO_2. The absorbance was read at 490 nm on the Microplate reader (GloMax® Discover Microplate Reader - Promega). Results were expressed as the percentage of MTS reduction relative to the control.

Hemolysis assay

The hemolysis test was performed as reported in the literature [12]. Briefly, venous blood (5 mL) was centrifuged at 500g for 5 minutes. The plasma was removed and replaced with 150 mM NaCl and the tube was centrifuged at 500g for 5 minutes (this procedure was repeated three times). The supernatant was replaced with PBS at pH 7.4. Subsequently 20 mL of diluted erythrocytes (1:50) were placed in a 50 mL tube, and several devices or 10 µL of 20% Triton X-100 were added (positive control) to the red blood cell. The tubes were incubated at 37°C for 4 hours and then centrifuged for 5 minutes at 500g. Then, 100µL of the supernatant was transferred to a transparent 96-well plate with a flat bottom and the absorbance, due to the presence of free hemoglobin, was read (490 nm) using a plate reader (GloMax® Discover Microplate Reader - Promega). After background subtraction, the absorbance of the positive control was determined. All experimental data were normalized with respect to the positive control, which was attributed 100% hemolysis.

Antibacterial test

Antibacterial test was performed according to the protocol reported elsewhere [12]. Briefly, the samples were sterilized under UV lamp at 254 nm for 1 hours. *Pseudomonas aeruginosa* was grown

in typical Luria-Bertani (LB) at 37 °C overnight (o.n.). Aliquots of the o.n. bacteria growth (500μL) were incubated in a tube to 50 mL containing LB (20 mL) for 120 min. Successively the bacteria, 150 μL, were gently dropped in the centre of the surface of the samples. After 1 h, the samples with bacteria were incubated in LB medium (20 mL) at 37 °C in agitation (200 rpm) and the bacterial growth was monitored spectrophotometrically. By spectrophotometric measurements, the exponential growth (600 nm) was analized by every 1 hour up to 4 hours. Data of three independent experiments were obtained.

Statistical analysis

The significance of the differences in the mean values of groups was evaluated using the analysis of variance (one-way ANOVA). The analysis was followed by Bonferroni's post hoc test. Differences were considered significant when the p-value was ≤ 0.05.

Results and discussion

Coating preparation: three-step process

Fig. 1a shows the growth curve (cell voltage vs. time) for the Ti6Al4V substrate anodized in CA and β-GPDS-containing solution at 20 mA cm^{-2}. During the early stages of anodizing process, the cell potential linearly depends on time indicating the growth of a barrier-type anodic oxide film [13].

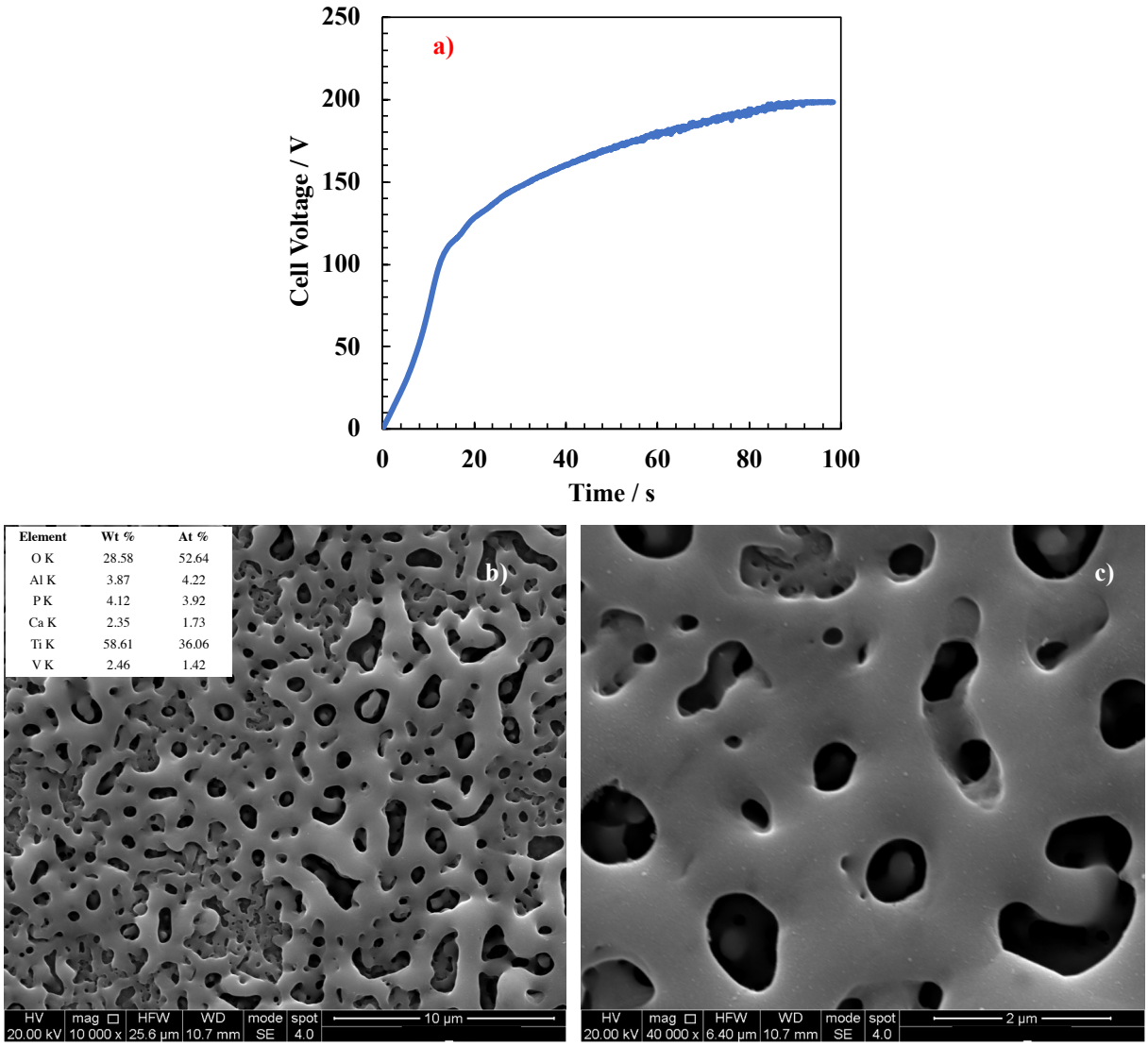

Figure 1. a) Cell voltage vs time curve related to the growth of the anodic oxide on Ti6Al4V alloy in CA and β-GPDS-containing solution. SEM micrographs related to anodized sample. b) 10000x magnification, c) 40000x magnification.

When cell potential is higher than ~ 50 V, the efficiency of the anodizing process decreases because of oxygen evolution reaction occurring. Much higher cell potential leads to the formation of an outer porous structure in a hard anodizing regime due to the dielectric breakdown of the oxide layer [14].

Fig. 1b and c shows SEM micrographs of the as anodized Ti6Al4V, disclosing a multiscale porous structure with a wide distribution of pores diameter. In contrast with previous results reported in the

literature for anodic layers grown in more concentrated CA and β-GPDS-containing solutions [3], the oxide is cracks free. EDX analysis reveals that the anodic layers contain Ti and O, but also Ca and P (Ca/P = 0.44). Incorporation of P can occur since the early stage of the anodizing process, since negatively charged phosphate ions are driven by the high electric field across the oxide toward the metal/oxide interface during the anodizing process. Conversely, positively charge Ca^{2+} ions are incorporated under the sparking regime due to local melting phenomena of TiO_2 and subsequent solidification once in contact with fresh electrolyte. As reported in ref. [14], the incorporation of calcium and phosphorus species can be also due to formation of colloidal solutions of polyphosphate complexes with di-, tri- or multivalent metal cations, such as $Ca_3P_6O_{18} \cdot xH_2O$ or $Na_2Ca_2P_6O_{18} \cdot xH_2O$, which are transformed to $CaO{\cdot}P_2O_5$ under the high temperatures and pressures at breakdown sites. Further, $(Ca_2P_6O_{18})^{2-}$ species may exist in the solution whose incorporation is assisted by the electric field during the anodizing process. Therefore, a Ca/P ranging between 0.33 and 0.5 is expected in in the anodic layer, which is close to that estimated by EDX.

X-ray diffraction of the as anodized samples reveals (101) reflection of TiO_2 anatase polymorph [15] (see Fig. 2a).

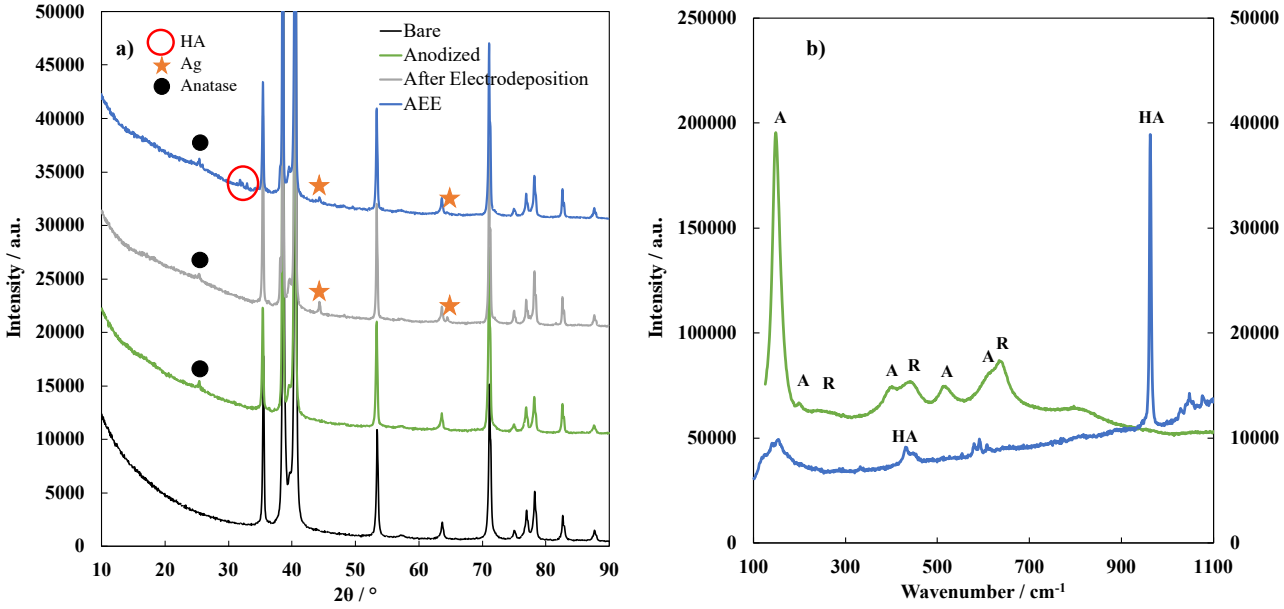

Figure 2. a) XRD diffractograms related to bare Ti6Al4V alloy, anodized sample before and after electrodeposition process and after electrophoretic deposition (AEE). b) Raman spectrum related to anodized sample (green line) and AEE sample (blue line). A: anatase, R: rutile polymorphs, HA: hydroxyapatite.

Its presence was also confirmed by Raman Spectroscopy (see Fig. 2b) together with the presence of rutile polymorph. The tetragonal structure of anatase belongs to the space group D_{4h} and has two formula units per primitive cell, leading to six Raman active phonons: $3E_g$ (144, 196 and 638 cm^{-1}), $2B1_g$ (398 and 519 cm^{-1}) and $1A1_g$ (513 cm^{-1}) [16]. Rutile has four Raman active modes: $1B1_g$ (143 cm^{-1}), E_g (235 and 447 cm^{-1}) and $A1_g$ (609 cm^{-1}). The Raman bands are shifted by a few cm^{-1} with respect to pure crystalline anatase phase, suggesting the formation of a defective TiO_2 layer. The presence of both TiO_2 polymorphs could be related to a higher bioactivity and cytocompatibility of the coating [15].

Anodizing was followed by Ag electrodeposition carried out galvanostatically imposing a cathodic current density of 1 mA cm^{-2}. Electrodeposition time was controlled in order to control the circulated charge and, thus, the amount of incorporated Ag. Fig. 3a shows the potential transient recorded during electrodeposition. Initial potential peak is usually related to the nucleation of electrodeposited metal whilst the second part of the potential vs time curve is usually related to the growth of deposited nuclei that can proceed at lower overpotential values [17]. The presence of Ag was confirmed by SEM micrographs of the samples (see Fig. 3b), by EDX analysis as well as by XRD diffraction.

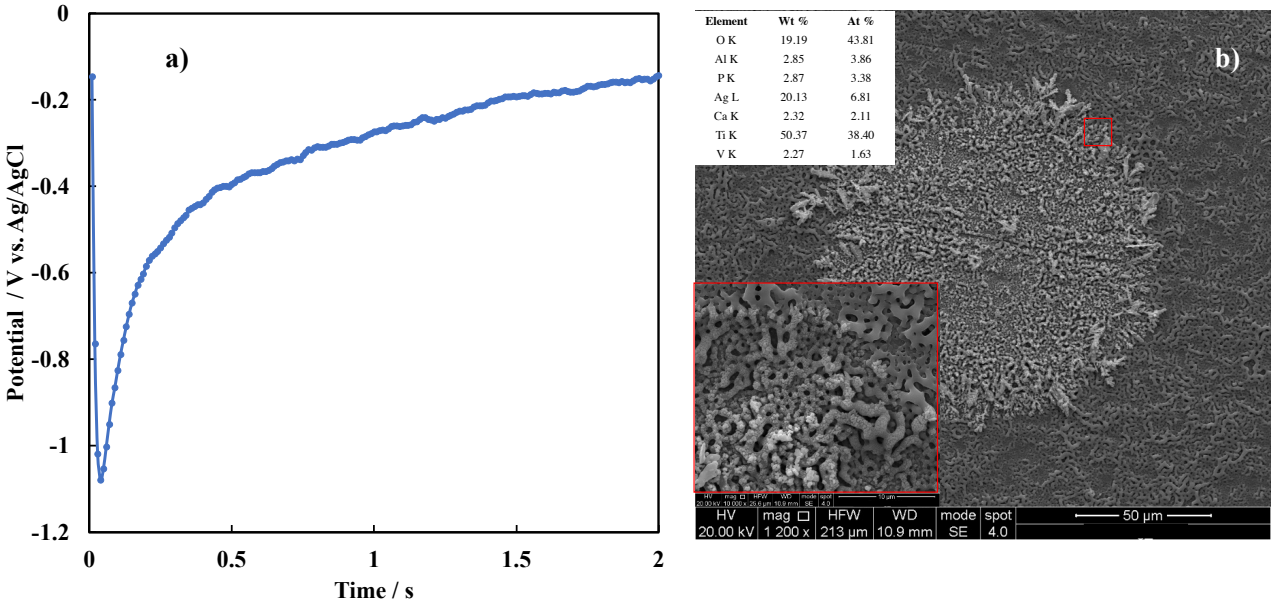

Figure 3. a) Potential vs. time curve recorded during Ag electrodeposition carried out galvanostatically at 1 mA cm^{-2} for 2 s. b) SEM micrograph related to the anodized Ti6Al4V sample after electrodeposition process.

Ag is present as aggregates at µm scale, composed by Ag nanoparticles [18]. These aggregates are not uniformly distributed along the whole sample, but Ag is still present since it is detected by EDX also in those areas where µm-sized aggregates miss.

Indeed, reflections of crystalline Ag are present in the diffraction pattern (see Fig. 2a) at 44° and 64.5° corresponding to (200) and (220) planes, respectively [19,20] . The amount of incorporated Ag into the coating was crucial to obtain long-term and efficient antibacterial properties and hemocompatibility without cytotoxicity. It is noteworthy to mention that these electrodeposition parameters (i.e. 1 mA cm^{-2} for 2 s) are the result of an optimization process of operating conditions. In fact, lower current density values led to samples without antibacterial properties. Therefore, we reported in the manuscript the electrodeposition operating conditions (i.e. minimum current density value) that guaranteed antibacterial properties, regardless if the sample is totally covered by Ag or not. However, the presence inside the pores of the anodic layer of alginic acid gel (see below) allows to slow down the release of Ag that, in high amount, can also become cytotoxic [21].

Finally, an electrophoretic deposition (AEE samples) step was carried out on Ag containing anodized samples by polarizing the electrodes at 7 V vs the counter electrode in an ethanol/water suspension containing HA microparticles (1 g L^{-1}) and sodium alginate (4 g L^{-1}). In spite the presence of a thick anodic layer under the imposed anodic potential, a significant current circulates across the electrode/electrolyte interface. The oxidation process sustaining this current is oxygen evolution, i.e.:

$$2H_2O \rightarrow O_2 + 4H^+ + 4e^- \quad (1)$$

with consequent hydrogen ions production inside the pores, since this reaction mainly occurs at the bottom of the pores where the electric field is higher. The electric field also drives negatively charge alginate ions toward the bottom of the pores, where they find an acidic environment and, since it is known that alginate solutions form gels at pH < 3 [22], the electrophoresis and neutralization of alginate ions in acidic region results in the formation of alginic acid (H–Alg) deposits starting from the bottom of the pores, according to the reaction (2)

$$Alg^- + H^+ \rightarrow H\text{-}Alg \quad (2)$$

At the same time, the electric field also drives HA particles inside the pores of the coatings since the latter carry a negative charge due to the adsorbed alginate ions. Such particles are embedded inside the alginic acid gel. The current density vs time transient recorded during potentiostatic deposition is reported in Fig. 4a), clearly showing that i decreases soon after the polarization in agreement with the ongoing pores' filling. The successful incorporation of HA particles is confirmed by the XRD patterns (see Fig. 2a) showing the reflections of hydroxyapatite [8], and by Raman Spectroscopy (see Fig. 2b). In particular, PO_4^{3-} features in HA are visible by ν_1 symmetric stretching (P-O) mode at 960 cm^{-1} and ν_2 bending vibrations at 438 cm^{-1} [23,24].

A significant change in the surface morphology is evident in the SEM micrographs reported in Fig. 4, showing the complete sealing of the porous structure.

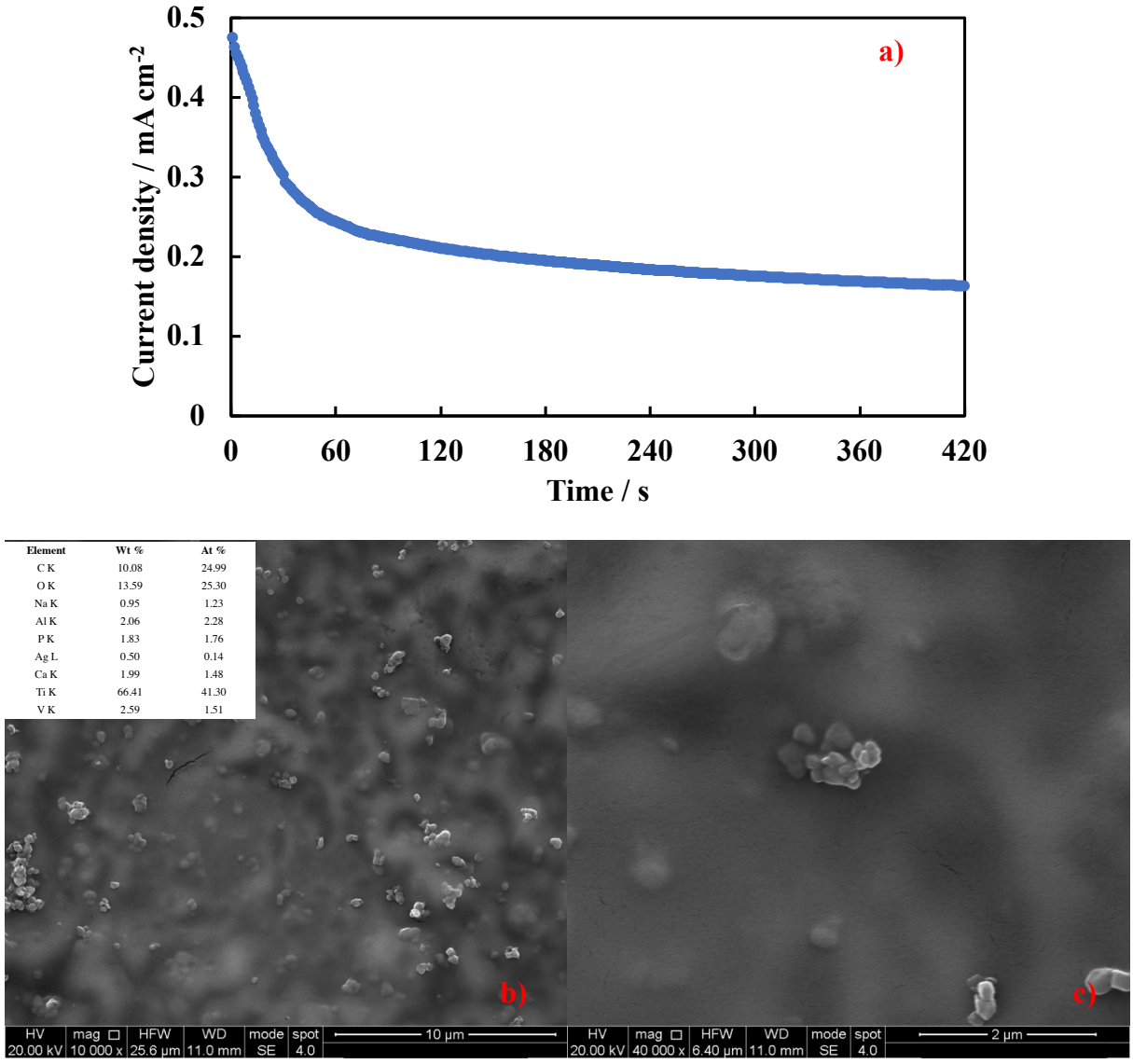

Figure 4. a) Current density vs time curve related to electrophoretic deposition of alginic acid. SEM micrograph related to the AEE sample after electrophoresis process: b) 10000x magnification, c) 40000x magnification.

EDX analysis revealed the presence of both Ca and P in a ratio of 0.85, which is lower than that of HA due to the signal arising from the anodic layer but higher than that measured before the electrophoretic deposition. Notably, signal arising from silver is still detected by XRD and EDX,

confirming that no loss of Ag occurs during the electrophoretic step (see Fig. 2a and 4b respectively).

Wettability of the samples was also assessed by water contact angle measurements. As it is possible to note from Fig. 5, a water contact angle of 64° was measured for bare Ti6Al4V. Water contact angle decreased after anodizing treatment and after electrophoresis process, measuring 29° and 8° respectively, therefore hydrophilicity was greatly enhanced, necessary to increase biocompatibility in terms of cell adhesion and proliferation [25,26]. This result can be rationalized by taking into account the presence of alginic acid gel, which is formed during electrophoresis process, that is highly hydrophilic [27], leading to lower water contact angle values.

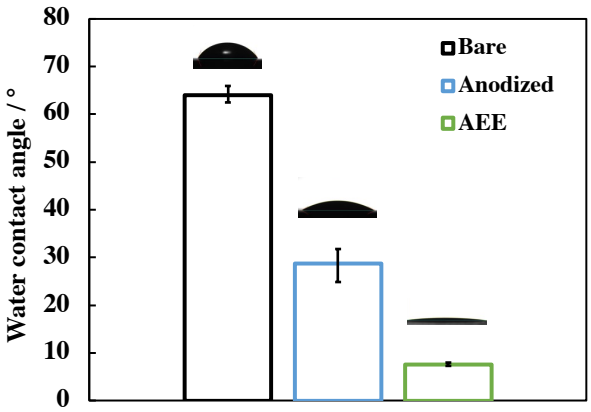

Figure 5. Water contact angle values of bare Ti alloy, anodized and AEE samples.

Electrochemical tests

The Ti6Al4V before and after electrochemical treatments were immersed in Hanks' solution 37°C and left at the open circuit potential (OCP) for 1 h. In order to get more information about the processes going on OCP, we recorded EIS spectra in the same solution (shown in Fig. 6 in the Nyquist representation), that were fitted using different equivalent circuits. The best fitting parameters are reported in Table 2. In the case of Ti6Al4V alloy covered by the air formed passive layer, the spectrum can be simulated by the simple one time constant Equivalent Electrical Circuit

(EEC) reported in Fig. 7, where R_P is the polarization resistance and is in parallel with Q_{ox}, accounts for the not ideal capacitance of the thin oxide layer. R_{el} is the electrolyte resistance.

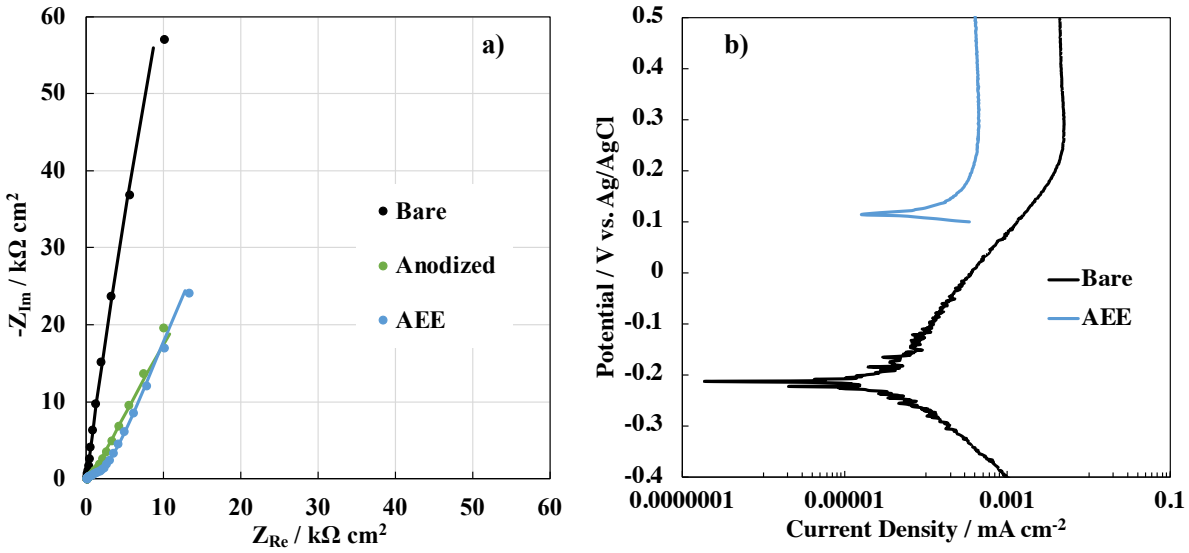

Figure 6. a) Nyquist representation of EIS spectra related to bare Ti6Al4V alloy, anodized sample and AEE sample recorded at corresponding E_{corr}. b) Polarization curves related to bare Ti6Al4V alloy and AEE sample recorded in Hanks' solution at 37°C.

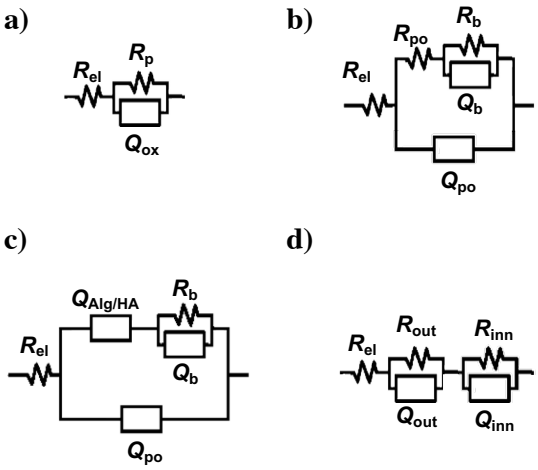

Figure 7. Equivalent electrical circuits (EECs) used to model the electrochemical behaviour of a) Bare Ti6Al4V alloy, b) anodized sample, c) AEE sample and d) samples after 1 month immersion in Hanks' solution.

	R_{el} [Ω cm^2]	R_p [Ω cm^2]	Q_{ox} [μS s^n cm^{-2}]	n	χ^2
Bare Ti6Al4V	17	1.77×10^6	27	0.92	9×10^{-4}

	R_{el} [Ω cm^2]	R_{po} [Ω cm^2]	Q_{po} [μS s^n cm^{-2}]	n	Q_b [μS s^n cm^{-2}]	n	R_b [Ω cm^2]	χ^2
Anodized	33	1500	21	0.69	42	0.72	5×10^5	3.2×10^{-3}

	R_{el} [Ω cm^2]	Q_{po} [μS s^n cm^{-2}]	n	$Q_{Alg/HA}$ [μS s^n cm^{-2}]	n	Q_b [μS s^n cm^{-2}]	n	R_b [Ω cm^2]	χ^2
AEE	25	0.37	0.91	162	0.25	64	0.85	4.5×10^5	6.7×10^{-4}

Table 2. Fitting parameters related to the impedance spectra shown in Fig. 7 recorded for the bare Ti6Al4V, anodized and AEE samples according to the EEC shown in Fig. 8a, 8b and 8c.

Air-formed passive film on the bare alloy has a high polarization resistance (~ 10^6) which explains the high bioinert character of the Ti6Al4V alloy. A completely different behaviour is shown by the anodized alloy and by the AEE sample. In fact, in accordance with the morphology of the samples (see before for the discussion on SEM micrographs), the electrochemical behaviour can be modelled with different EECs. As for anodized alloy, the EEC is shown in Fig. 7b and comprises Q_{po}, a CPE modelling the pore wall non ideal capacitance, in parallel with a series between R_{po}, the electrolyte resistance inside the pore, and the (R_b Q_b) parallel, related to the barrier oxide layer presence at the bottom of the pore. Corresponding fitting parameters are reported in Table 2.

A different EEC (see Fig. 7c) must be employed to model the electrochemical behaviour of AEE sample soon after the fabrication process. In this case, despite the pore structure is analogue to that of the anodized sample, the pore is filled with HA embedded in alginic acid gel. In this case, the deposition products inside the pore were modelled with a $Q_{Alg/HA}$ CPE element, accounting for a series of parallels (RC), i.e. a distribution of time constants along the pore modelling the complex structure of HA/alginic acid gel [28]. Fitting parameters are reported in Table 2.

Overall impedance related to both anodized and AEE samples are lower with respect to bare Ti6Al4V alloy sample, thus suggesting that the anodic layer grown on Ti6Al4V alloy is less insulating with respect to air formed passive film in agreement with previous findings reported in the literature [29]. From a synergistic electrochemical and photoelectrochemical characterization, it was noted that for a thick anodic oxide grown on Ti6Al4V (as that studied in this work), corrosion potential is more cathodic than oxide flat band potential. Therefore, in free corrosion conditions as when the sample is immersed in Hanks' solution, the anodic layer is polarized in forward bias regime leading to a less blocking behaviour toward oxidation/reduction reactions [29]. This behaviour is also confirmed by the polarization curves recorded in Hanks' solution at 37°C for bare Ti6Al4V alloy and for AEE sample (see Fig. 6b). The multifunctional coating shifts the corrosion potential toward more positive value, but the corrosion current density is comparable or even higher than that estimated for bare alloy. This indicates that during immersion in Hanks' solution the coating does not hinders the reactivity of the material.

In order to assess the effect of surface treatment and of immersion time on the HA growth, Ti6Al4V alloys after anodizing and after the three-step process were immersed in Hanks' solution at 37°C. Fig. 8 shows the surface morphology for these samples after 1 month of immersion time.

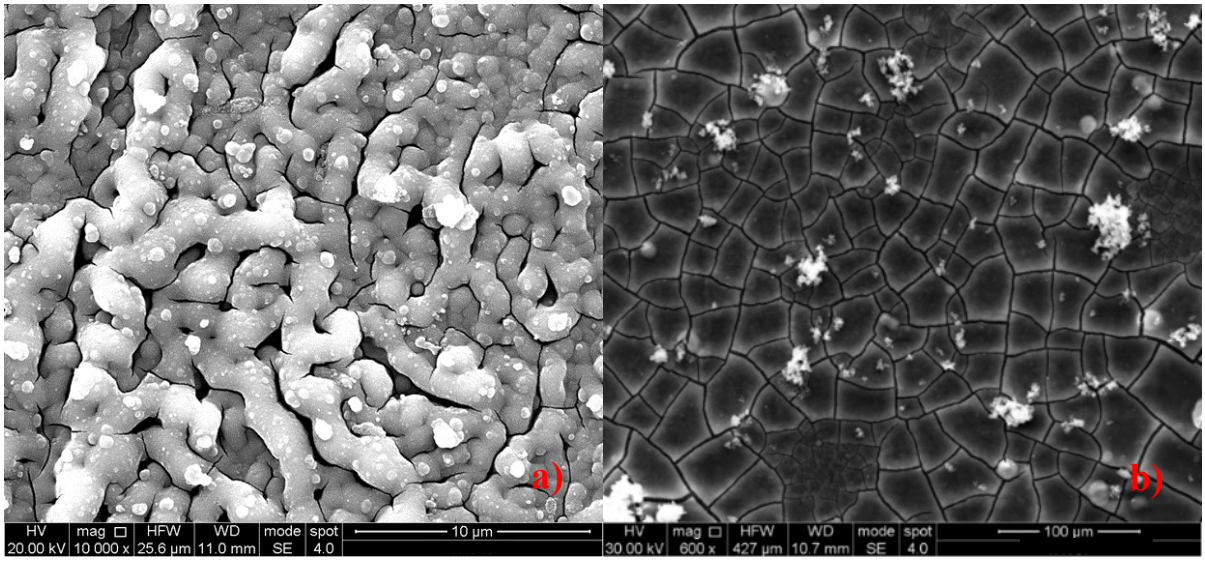

Figure 8. SEM micrograph related to a) anodized and b) AEE sample after 1 month of immersion in Hanks' solution.

In the case of the anodized sample, there is evidence of HA precipitation. In fact, the porous structure of the anodic layer resulted to be almost completely filled with clear evidence of HA on the surface of the coating (see Fig. 8a). In the case of the Ti6Al4V sample treated with the three-step electrochemical process, HA was present soon after the end of the fabrication process as already stated (see Fig. 4). After 1 month as immersion time the typical "mud" structure related to the presence of a thick HA layer can be seen on the surface. HA presence is also confirmed by Raman spectrum reported in Fig. S1. These observations based on SEM micrographs were also used to properly modelling the electrochemical behaviour of the systems to fit the impedance spectra reported in Fig. 9.

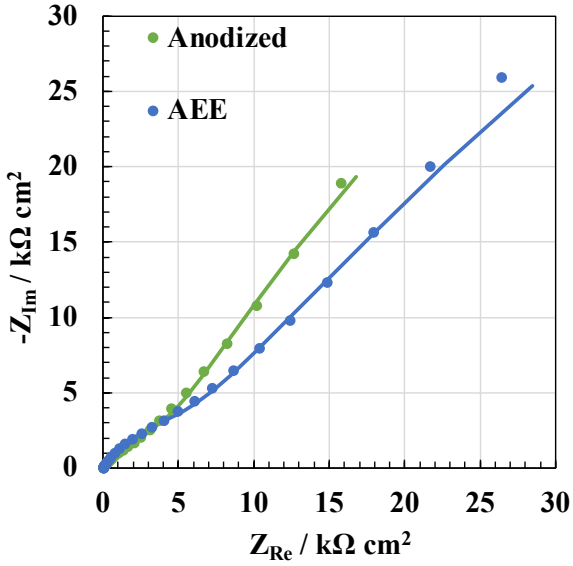

Figure 9. Nyquist representation of EIS spectra related to anodized sample and AEE sample after 1 month in Hanks' solution recorded at corresponding E_{corr}. Fitting according to EEC shown in Fig. 7d.

In this case, both impedance spectra related to anodized and AEE samples were fitted according to the EEC reported in Fig. 7d, i.e. R_{el} in series with two parallels (RQ), (R_{inn} Q_{inn}) and (R_{out} Q_{out}) accounting for the morphology of the system that, after 1 month of immersion in Hanks' solution, can be assumed as the series of two compact layers. This is the consequence of the fact that there is an internal filled porous structure covered by a HA layer, thicker in the case of AEE sample immersed for 1 month. Fitting parameters are reported in Table 3. Overall impedance decreased with immersion time indicating the bioactivity of the AEE sample with a thicker layer of HA, necessary for a proper osteointegration of the biomedical device.

	R_{el} [Ω cm²]	Q_{out} [μS sⁿ cm⁻²]	n	R_{out} [Ω cm²]	Q_{inn} [μS sⁿ cm⁻²]	n	R_{inn} [Ω cm²]	χ^2
Anodized	18	29	0.56	5000	57	0.73	1.4×10^5	1.4×10^{-3}
AEE	21	9.3	0.68	4500	34	0.57	3.0×10^5	1.4×10^{-3}

Table 3. Fitting parameters (out: outer layer, inn: inner layer) related to the impedance spectra shown in Fig. 9 recorded for the bare Ti6Al4V, anodized and AEE samples according to the EEC shown in Fig. 7d.

Based on the reported results, it is possible to note that the three-step electrochemical process provides a route for a smart functionalization of Ti6Al4V alloys. Reported bioactivity is peculiar of the AEE sample and is the consequence of a tailored electrochemical process. In fact, the anodizing process allows to cover the alloy surface with a thick porous and well adherent TiO_2 layer. Such porous film provides a good pattern for hosting Ag, whose release rate in turn is slowed down due to the sealing of pores with a HA containing alginic acid gel deposited during the electrophoresis. The latter can uptake Hanks' solution during immersion, thus the bottom of the porous anodic film is in contact with the electrolyte even if sealed by the biopolymer. The bioactivity of AEE sample can be explained by an increased reactivity that leads to the growth of HA with immersion in Hanks' solution. In fact, at the corrosion potential, the half cell cathodic process is O_2 reduction, i.e.:

$$O_2 + 4e^- + 2H_2O \rightarrow 4OH^- \quad (3)$$

The reaction produces OH^- and therefore alkalinization occurs at the bottom of the pores. The half cell anodic process is Ti oxidation from the alloy beneath or the oxidation of Ti^{x+} ($x < 4$) to Ti^{4+} contained in the oxide compensating the Ti lost from the layer due to dissolution phenomena. According to ref. [14], for the anodic layers prepared in calcium and phosphate containing solutions, Ca^{2+} ions and Ti^{4+} ions are released during immersion in Hanks' solution with a higher rate for the former ions. Therefore, the simultaneous production of OH^- due to reaction (3) and the release of Ca^{2+} ions favours the precipitation of HA according to the following equations [8]:

$$10Ca^{2+} + 8OH^- + 6HPO_4^{2-} \rightarrow Ca_{10}(PO_4)_6(OH)_2 + 6H_2O \quad (4a)$$

$$10Ca^{2+} + 6PO_4^{3-} + 2OH^- \rightarrow Ca_{10}(PO_4)_6(OH)_2 \quad (4b)$$

Cytocompatibility

After the three-step process, Ti6Al4V samples must first be tested *in vitro* to ensure that cell viability is not compromised. To test for a possible toxic effect due to components that can be released from the device made in Ti6Al4V during prolonged application such as for the bone implant, a viability test was carried out using the cell medium in which the different samples were incubated separately (extract test). The medium was collected at different times, within a two-week period, and administered to the 3T3 fibroblast cells. Fibroblast were used as a model to measure the in vitro cell viability of biomaterials used for implants for the human body [30,31]. Results were analyzed according to the ISO10993-5 standard guidelines [32,33]. By morphological inspection, cells showed normal morphology (no toxic response including detachment, lysis, extensive vacuolization, reduction of cell growth) and no change in their number and can be classified of grade 0 [32,33]. (Figure 10a). Moreover, after the treatments the cells were submitted to one of the most common tests used, the MTS test [32,33]. MTS assay is based on the measure of the mitochondrial metabolic activity and is routinely used as index of cellular viability and proliferation. According to the ISO10993-5 guidelines, a biomaterial is considered cytotoxic when its viability is below 70% (Figure 10b). After exposure of 3T3 fibroblast cells to conditioned cell medium for 48 h, we found 100% cell viability, for all the samples at all exposure times, indicating that there is no release of any substances that induce cell toxicity or abnormal cell growth.

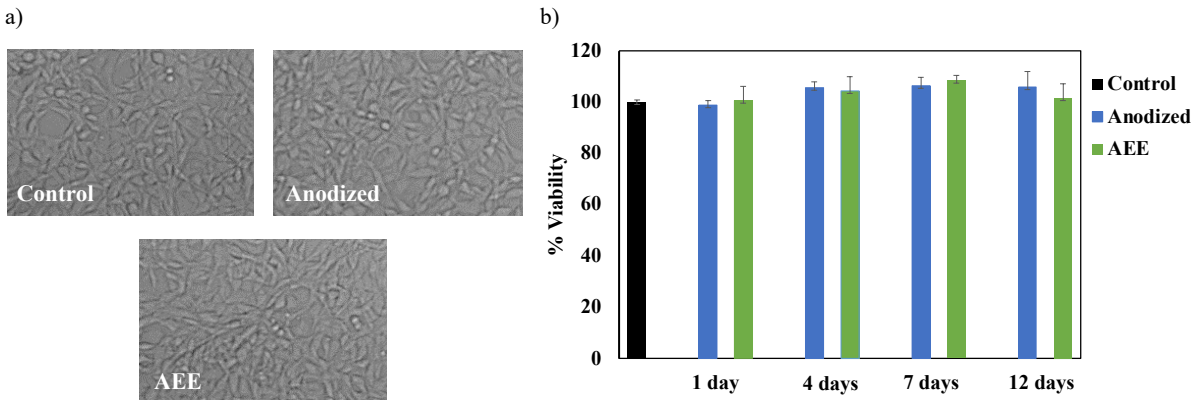

Figure 10. Cytocompatibility analysis. a) Morphological images of 3T3 cells: untreated (Control) or treated with cellular medium in which Ag and No Ag samples were immersed for 12 days. b) MTS viability assay of 3T3 cells treated with the cellular medium in which Ag and No Ag samples were immersed for different times (1, 4, 7, 12 days).

Hemocompatibility

The insertion of bone implants causes a vascular trauma to the bone, with the break of the blood vessels and following contact of the implant with the blood [34]. *In vitro* hemocompatibility is one of the biological evaluations recommended by ISO 10993-4 guidelines for the medical devices [35]. In particular, erythrocytes wellness or destruction is a hemocompatibility index. To evaluate this effect, the samples were incubated with erythrocytes for 4 h. Hemocompatibility tests were carried out for bare Ti6Al4V samples, after the anodizing process and after the complete three-step process. As shown in Fig. 11, hemolysis ratio was analysed by using a spectrophotometrical test, which measures the amount of free plasma Hemoglobin (Hb). In Fig. 11a is evidenced that the hemolysis percentage induced by the presence of the biomaterials in the blood sample was comparable to the untreated control, whereas whole hemolysis was observable in the sample treated with Triton-X, used as positive control. To confirm the results, photographs of the tubes of untreated human

erythrocytes, incubated with the positive control (tritonx100) and with the different samples after centrifugation, were also shown (Fig. 11b). The result was supported by erythrocyte microscopic analysis, where the morphology of the treated erythrocytes is similar to the control (untreated) (Fig. 11c). Test results confirmed the hemocompatibility of the samples treated with the three-step process.

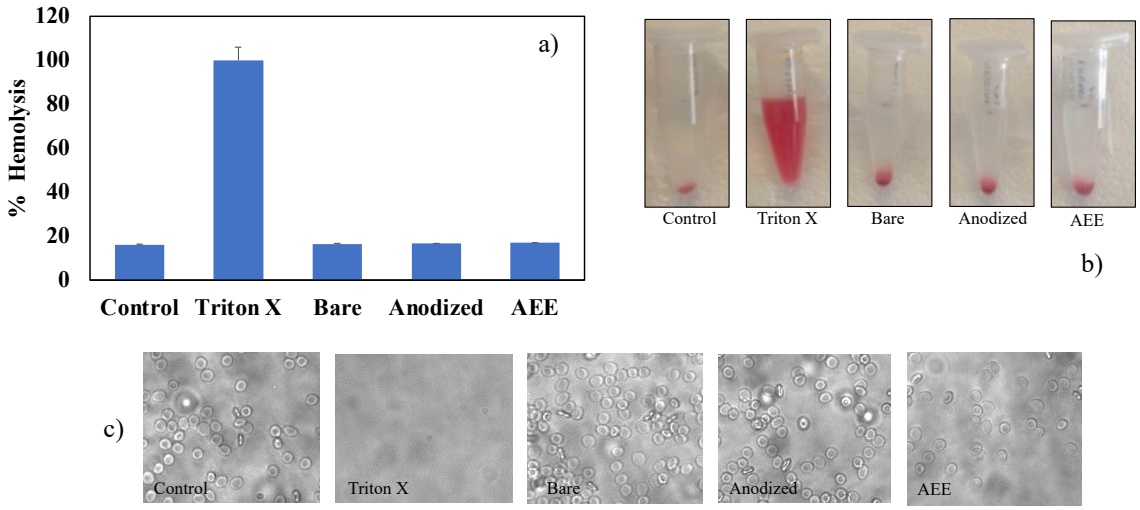

Figure 11. Hemocompatibility analysis. a) Histogram relative to the absorbance of released Hb after treatment with the different samples. The values are expressed as the percentage respect to the positive control (TritonX), $p < 0.05$ vs control. b) Photographs of the tubes of human erythrocytes untreated, incubated with the positive control (tritonx100) and with the different samples after centrifugation. c) Microscopic images of hemolysis assay of erythrocytes (Control) or incubated with Triton-X (positive control) and with the different samples.

Bacterial growth and adhesion

Implant-associated infections are a major problem in surgery. Bacteria have the potential to adhere to the implant, grow and develop to form biofilms [36]. There is great interest in new methods of coating bone implants that reduce bacterial colonization (adhesion) or release antimicrobial agents

from the implant surface resulting in improved survival of bone implants [37]. There are multifunctional technologies that combine both of the aforementioned approaches, anti-adhesive and antimicrobial agents. *Pseudomonas arginouse* bacteria were used to study the antibacterial effects of the samples before and after anodizing process and after the whole three-step process. Aliquots of the o.n. bacteria growth were incubated in a tube containing LB for 120 min. Successively the bacteria were gently dropped in the center of the surface of the samples. After 1h, the sample with bacteria were incubated in LB medium and the bacterial growth was monitored spectrophotometrically every 1 h (Fig. 12a) [38].The difference in the growth curves for the tube containing the samples with Ag were detected with respect to the bare Ti6Al4V alloy and anodized Ti6Al4V samples. The results indicating that the Ag deposited through the electrodeposition process provides high antibacterial properties (Fig. 12b). This effect is also clearly evident from the photographs of the tubes, where in the tube with the samples containing Ag the bacterial culture medium is clear, indicating an absence of bacterial growth (see Fig. 12c). Antibacterial effect it might be based on the release of silver cations from Ti6Al4V surface.

These cations disrupt bacterial wall, cause DNA alteration, lead to reacting oxygen species production and inactivate essential proteins [39].

Bacterial adhesion was also investigated by SEM analysis. Experimental results (Fig. 12d) indicated that bacteria were present only on bare Ti6Al4V alloy, indicating that the coating has anti-adhesive bacterial properties. Hydrophilic, highly hydrated, and non-charged surfaces have been shown *in vitro* to prevent many bacterial adhesion by limiting the contact between bacterium and potential surface placement sites [40]. In an effort to better, understand these events, biomaterials that exhibit multiple properties, namely antimicrobial agents that can be released and reduced bacterial adhesiveness, have become an important area of research.

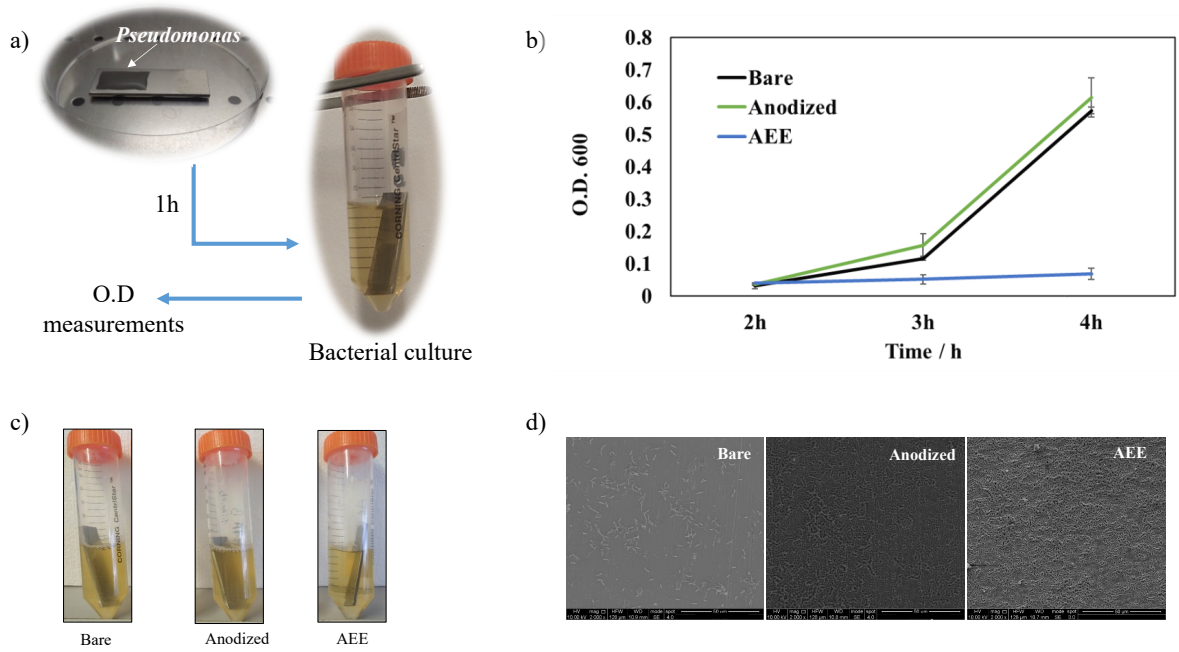

Figure 12. Antimicrobial and antiadhesion properties. a) Schematic representation of bacteria experiment. The bacteria were gently dropped in the center of the surface of the biomaterials slide. After 1 h, the biomaterial with bacteria were incubated in LB medium and the bacterial growth was monitored spectrophotometrically. b) Histogram of optical density (O.D.600) measured every 1 h, c) photographs tubes containing the bacterial after 4 h and d) SEM image of bacteria adhesion of the devices after 4 h.

Conclusions

A three-step electrochemical process was proposed to fabricate a coating on Ti6Al4V alloy tailoring its morphology, composition and, thus, the bioactivity of the alloy for biomedical applications. The process comprised an anodizing step to grow a thick porous oxide on the Ti6Al4V alloy, an electrodeposition step to deposit Ag nanoparticles to give antibacterial properties to the coating, and a final electrophoretic step to deposit alginate and hydroxyapatite into the porous structure of the coating. The final coating was characterized in Hanks' solution to verify the compatibility with the

human body environment in terms of suitable hydroxyapatite growth to enhance the osteointegration of the initial Ti6Al4V alloy. The characteristics of the coating were verified also after 1 month of immersion time in Hanks' solution through EIS spectra and SEM microscopy confirming a decreased barrier layer resistance and the thickening of outer hydroxyapatite layer with the formation of the "typical" mud structure.

We also demonstrated that Ti6Al4V alloy treated with the three-step process is cytocompatible, hemocompatible and has antibacterial properties unlike bare alloy and anodized sample.

References

[1] B. Zhang, J. Li, L. He, H. Huang, J. Weng, Bio-surface coated titanium scaffolds with cancellous bone-like biomimetic structure for enhanced bone tissue regeneration, Acta Biomater. 114 (2020) 431–448. https://doi.org/10.1016/j.actbio.2020.07.024.

[2] E. Estrada-Cabrera, L.R. Torres-Ferrer, O.G. Aztatzi-Aguilar, A. De Vizcaya-Ruiz, M.A. Meraz-Rios, D.G. Zarate-Triviño, A. Arizmendi-Morquecho, A. de Luna Bugallo, E. Prokhorov, G. Luna-Barcenas, Chitosan-bioglass coatings on partially nanostructured anodized Ti-6Al-4V alloy for biomedical applications, Surf. Coatings Technol. 375 (2019) 468–476. https://doi.org/10.1016/j.surfcoat.2019.07.002.

[3] A.C. Alves, F. Wenger, P. Ponthiaux, J.P. Celis, A.M. Pinto, L.A. Rocha, J.C.S. Fernandes, Corrosion mechanisms in titanium oxide-based films produced by anodic treatment, Electrochim. Acta. 234 (2017) 16–27. https://doi.org/10.1016/j.electacta.2017.03.011.

[4] T. Moskalewicz, M. Warcaba, Ł. Cieniek, M. Sitarz, M. Gajewska, A.R. Boccaccini, Hydroxyapatite/sodium alginate coatings electrophoretically deposited on titanium substrates: microstructure and properties, Appl. Surf. Sci. 540 (2021). https://doi.org/10.1016/j.apsusc.2020.148353.

[5] S. V. Harb, N.J. Bassous, T.A.C. de Souza, A. Trentin, S.H. Pulcinelli, C. V. Santilli, T.J.

Webster, A.O. Lobo, P. Hammer, Hydroxyapatite and β-TCP modified PMMA-TiO2 and PMMA-ZrO2 coatings for bioactive corrosion protection of Ti6Al4V implants, Mater. Sci. Eng. C. 116 (2020) 111149. https://doi.org/10.1016/j.msec.2020.111149.

[6] B.L. Pereira, G. Beilner, C.M. Lepienski, E.S. Szameitat, B.S. Chee, N.K. Kuromoto, L.L. dos Santos, I. Mazzaro, A.P.R.A. Claro, M.J.D. Nugent, Oxide coating containing apatite formed on Ti-25Nb-25Ta alloy treated by Two-Step Plasma Electrolytic Oxidation, Surf. Coatings Technol. 382 (2020). https://doi.org/10.1016/j.surfcoat.2019.125224.

[7] V. Müller, T. Pagnier, S. Tadier, L. Gremillard, M. Jobbagy, E. Djurado, Design of advanced one-step hydroxyapatite coatings for biomedical applications using the electrostatic spray deposition, Appl. Surf. Sci. 541 (2021). https://doi.org/10.1016/j.apsusc.2020.148462.

[8] V.T. Nguyen, T.C. Cheng, T.H. Fang, M.H. Li, The fabrication and characteristics of hydroxyapatite film grown on titanium alloy Ti-6Al-4V by anodic treatment, J. Mater. Res. Technol. 9 (2020) 4817–4825. https://doi.org/10.1016/j.jmrt.2020.03.002.

[9] H. Ishizawa, M. Fujino, M. Ogino, Histomorphometric evaluation of the thin hydroxyapatite layer formed through anodization followed by hydrothermal treatment, J. Biomed. Mater. Res. 35 (1997) 199–206. https://doi.org/10.1002/(SICI)1097-4636(199705)35:2<199::AID-JBM8>3.0.CO;2-I.

[10] H. Ishizawa, M. Ogino, Formation and characterization of anodic titanium oxide films containing Ca and P, J. Biomed. Mater. Res. 29 (1995) 65–72. https://doi.org/10.1002/jbm.820290110.

[11] S. Yu, D. Guo, J. Han, L. Sun, H. Zhu, Z. Yu, M. Dargusch, G. Wang, Enhancing Antibacterial Performance and Biocompatibility of Pure Titanium by a Two-Step Electrochemical Surface Coating, ACS Appl. Mater. Interfaces. 12 (2020) 44433–44446. https://doi.org/10.1021/acsami.0c10032.

[12] P. Picone, M.A. Sabatino, A. Ajovalasit, D. Giacomazza, C. Dispenza, M. Di Carlo, Biocompatibility, hemocompatibility and antimicrobial properties of xyloglucan-based

hydrogel film for wound healing application, Int. J. Biol. Macromol. 121 (2019) 784–795. https://doi.org/10.1016/j.ijbiomac.2018.10.078.

[13] A. Zaffora, F. Di Franco, D. Virtù, F. Carfì Pavia, G. Ghersi, S. Virtanen, M. Santamaria, Tuning of the Mg Alloy AZ31 Anodizing Process for Biodegradable Implants, ACS Appl. Mater. Interfaces. 13 (2021) 12866–12876. https://doi.org/10.1021/acsami.0c22933.

[14] E. Matykina, M. Montuori, J. Gough, F. Monfort, A. Berkani, P. Skeldon, G.E. Thompson, H. Habazaki, Spark anodising of titanium for biomedical applications, Trans. Inst. Met. Finish. 84 (2006) 125–133. https://doi.org/10.1179/174591906X123967.

[15] H.N. Pantaroto, J.M. Cordeiro, L.T. Pereira, A.B. de Almeida, F.H. Nociti Junior, E.C. Rangel, N.F. Azevedo Neto, J.H.D. da Silva, V.A.R. Barão, Sputtered crystalline TiO2 film drives improved surface properties of titanium-based biomedical implants, Mater. Sci. Eng. C. 119 (2021). https://doi.org/10.1016/j.msec.2020.111638.

[16] D. Georgescu, L. Baia, O. Ersen, M. Baia, S. Simon, Experimental assessment of the phonon confinement in TiO2 anatase nanocrystallites by Raman spectroscopy, J. Raman Spectrosc. 43 (2012) 876–883. https://doi.org/10.1002/jrs.3103.

[17] D.A. Crespo-Yapur, A.S. Elizondo, D. Herrera, M. Videa, Galvanostatic electrodeposition of silver nanoparticles: Nucleation and growth studies, Mater. Today Proc. 48 (2022) 1–4. https://doi.org/10.1016/j.matpr.2020.04.760.

[18] Y.S. Hedberg, F. Gamna, G. Padoan, S. Ferraris, M. Cazzola, G. Herting, M. Atapour, S. Spriano, I. Odnevall Wallinder, Surface modified Ti6Al4V for enhanced bone bonding ability – Effects of silver and corrosivity at simulated physiological conditions from a corrosion and metal release perspective, Corros. Sci. 168 (2020) 108566. https://doi.org/10.1016/j.corsci.2020.108566.

[19] H. Singh, J. Du, P. Singh, T.H. Yi, Ecofriendly synthesis of silver and gold nanoparticles by Euphrasia officinalis leaf extract and its biomedical applications, Artif. Cells, Nanomedicine Biotechnol. 46 (2018) 1163–1170. https://doi.org/10.1080/21691401.2017.1362417.

[20] B.K. Mehta, M. Chhajlani, B.D. Shrivastava, Green synthesis of silver nanoparticles and their characterization by XRD, J. Phys. Conf. Ser. 836 (2017). https://doi.org/10.1088/1742-6596/836/1/012050.

[21] T. Akiyama, H. Miyamoto, Y. Yonekura, M. Tsukamoto, Y. Ando, I. Noda, M. Sonohata, M. Mawatari, Silver oxide-containing hydroxyapatite coating has in vivo antibacterial activity in the rat tibia, J. Orthop. Res. 31 (2013) 1195–1200. https://doi.org/10.1002/jor.22357.

[22] D. Zhitomirsky, J.A. Roether, A.R. Boccaccini, I. Zhitomirsky, Electrophoretic deposition of bioactive glass/polymer composite coatings with and without HA nanoparticle inclusions for biomedical applications, J. Mater. Process. Technol. 209 (2009) 1853–1860. https://doi.org/10.1016/j.jmatprotec.2008.04.034.

[23] J.A. Stammeier, B. Purgstaller, D. Hippler, V. Mavromatis, M. Dietzel, In-situ Raman spectroscopy of amorphous calcium phosphate to crystalline hydroxyapatite transformation, MethodsX. 5 (2018) 1241–1250. https://doi.org/10.1016/j.mex.2018.09.015.

[24] V. V. Nosenko, A.M. Yaremko, V.M. Dzhagan, I.P. Vorona, Y.A. Romanyuk, I. V. Zatovsky, Nature of some features in Raman spectra of hydroxyapatite-containing materials, J. Raman Spectrosc. 47 (2016) 726–730. https://doi.org/10.1002/jrs.4883.

[25] C. Zhu, Y. Lv, C. Qian, Z. Ding, T. Jiao, X. Gu, E. Lu, L. Wang, F. Zhang, Microstructures, mechanical, and biological properties of a novel Ti-6V-4V/zinc surface nanocomposite prepared by friction stir processing, Int. J. Nanomedicine. 13 (2018) 1881–1898. https://doi.org/10.2147/IJN.S154260.

[26] L. Hong, L. Yuan, X. Xu, Y. Ma, L. Meng, J. Wang, N. Zhao, X. Wang, J. Ma, Biocompatible Nanotube-Strontium/polydopamine-arginine–glycine–aspartic acid coating on Ti6Al4V enhances osteogenic properties for biomedical applications, Microsc. Res. Tech. 85 (2022) 1518–1526. https://doi.org/10.1002/JEMT.24014.

[27] M.I. Neves, L. Moroni, C.C. Barrias, Modulating Alginate Hydrogels for Improved Biological Performance as Cellular 3D Microenvironments, Front. Bioeng. Biotechnol. 8

(2020). https://doi.org/10.3389/fbioe.2020.00665.

[28] F. Di Franco, A. Zaffora, P. Vassallo, M. Santamaria, Double Step Electrochemical Process for the Deposition of Superhydrophobic Coatings for Enhanced Corrosion Resistance, J. Electrochem. Soc. 168 (2021) 101502. https://doi.org/10.1149/1945-7111/ac29df.

[29] F. Di Franco, A. Zaffora, D. Pupillo, L. Iannucci, S. Grassini, M. Santamaria, The Effect of Electronic Properties of Anodized and Hard Anodized Ti and Ti6Al4V on Their Reactivity in Simulated Body Fluid, J. Electrochem. Soc. 169 (2022) 071506. https://doi.org/10.1149/1945-7111/AC8316.

[30] X. He, K. Tang, X. Li, F. Wang, J. Liu, F. Zou, M. Yang, M. Li, A porous collagen-carboxymethyl cellulose/hydroxyapatite composite for bone tissue engineering by bi-molecular template method, Int. J. Biol. Macromol. 137 (2019) 45–53. https://doi.org/10.1016/j.ijbiomac.2019.06.098.

[31] V. Babuska, J. Dobra, V. Kulda, M. Kripnerova, A. Moztarzadeh, L. Bolek, J. Lahoda, D. Hrusak, Comparison of fibroblast and osteoblast response to cultivation on titanium implants with different grain sizes, J. Nanomater. 2015 (2015). https://doi.org/10.1155/2015/920893.

[32] A. Bruinink, R. Luginbuehl, Evaluation of biocompatibility using in vitro methods: interpretation and limitations., Adv. Biochem. Eng. Biotechnol. 126 (2012) 117–152. https://doi.org/10.1007/10_2011_111.

[33] ISO 10993-5 Biological Evaluation of Medical Devices. Part 5: Tests for in Vitro Cytotoxicity, (2009).

[34] F. Rupp, L. Liang, J. Geis-Gerstorfer, L. Scheideler, F. Hüttig, Surface characteristics of dental implants: A review, Dent. Mater. 34 (2018) 40–57. https://doi.org/10.1016/j.dental.2017.09.007.

[35] ISO 10993-4 Biological evaluation of medical devices — Part 4: Selection of tests for interactions with blooditle, (2002).

[36] T.F. Moriarty, S.A.J. Zaat, H.J. Busscher, Biomaterials associated infection: Immunological

aspects and antimicrobial strategies, 2013. https://doi.org/10.1007/978-1-4614-1031-7.

[37] J.D. Caplin, A.J. García, Implantable antimicrobial biomaterials for local drug delivery in bone infection models, Acta Biomater. 93 (2019) 2–11. https://doi.org/10.1016/j.actbio.2019.01.015.

[38] M. Contardi, D. Kossyvaki, P. Picone, M. Summa, X. Guo, J.A. Heredia-Guerrero, D. Giacomazza, R. Carzino, L. Goldoni, G. Scoponi, F. Rancan, R. Bertorelli, M. Di Carlo, A. Athanassiou, I.S. Bayer, Electrospun polyvinylpyrrolidone (PVP) hydrogels containing hydroxycinnamic acid derivatives as potential wound dressings, Chem. Eng. J. 409 (2021). https://doi.org/10.1016/j.cej.2020.128144.

[39] M.L.W. Knetsch, L.H. Koole, New strategies in the development of antimicrobial coatings: The example of increasing usage of silver and silver nanoparticles, Polymers (Basel). 3 (2011) 340–366. https://doi.org/10.3390/polym3010340.

[40] L. Rojo, J.M. Barcenilla, B. Vázquez, R. González, J. San Román, Intrinsically antibacterial materials based on polymeric derivatives of eugenol for biomedical applications, Biomacromolecules. 9 (2008) 2530–2535. https://doi.org/10.1021/bm800570u.